Supporting Information

Exceptionally low charge trapping enables highly efficient organic bulk heterojunction solar cells

Jiaying Wu,[†a], Jinho Lee,[†ab], Yi-Chun Chin,[b] Huifeng Yao,[c] Hyojung Cha,[a] Joel Luke,[b] Jianhui Hou,[c] Ji-Seon Kim*[b] and James R. Durrant*[ad]

a. Department of Chemistry and Centre for Processable Electronics, Imperial College London, White City Campus, London, W12 0BZ, UK
e-mail: j.durrant@imperial.ac.uk

b. Department of Physics and Centre for Processable Electronics, Imperial College London, South Kensington Campus, London, SW7 2AZ, UK
e-mail: ji-seon.kim@imperial.ac.uk

c. State Key Laboratory of Polymer Physics and Chemistry, Institute of Chemistry, Chinese Academy of Sciences, 100190 Beijing, China

d. SPECIFIC, College of Engineering, Bay Campus, Swansea University, Swansea, SA1 8EN, UK

† These authors contributed equally to this work.

Experimental section:

Device preparation:
PM6:Y6 OSCs were fabricated with an inverted structure of ITO/zinc oxide (ZnO)/PM6:Y6/molybdenum oxide (MoO_3)/Ag. The sol-gel based ZnO precursor solution was prepared by dissolving 220mg of zinc acetate dehydrate in 60 µl of ethanolamine and 2 ml of 2-methoxyethanol[1]. The PM6 and Y6 were synthesized according to the methods in the previous work[5]. The ZnO solution was spin-coated at 4000 rpm on the pre-cleaned ITO substrate. Subsequently, the samples were annealed at 150 °C for 20 min in air and then transferred into an N_2-filled glove box for spin-coating of the photoactive layers. The PM6:Y6 (1:1.2) layers were deposited from 7 mg ml^{-1} chlorobenzene/ chloronaphthalene (CN) (99.5:0.5 vol%) solution by spin-coating at 2000 rpm and then annealed at 100 °C for 10 min. Finally, the MoO_3 (10 nm) and Ag (100 nm) layers were deposited by thermal evaporation under high vacuum condition through a shadow mask yielding active areas of 0.045 cm^2 in each device.

Current-voltage (*J_V*) characterisation and cyclic voltammetry (CV):
J_V characteristic was performed by a Keithley 2400 source meter under both solar simulators (Newport 92193A-1000) with the intensity of a 100 mW/cm^2 using a 150W ozone free Xenon arc lamp Sciencetech 200 series with a water-cooled IR filter. The illumination is calibrated using a silicon photodiode. CV measurements were carried out using an Electrochemical Analyzer (Metrohm Autolab PGSTAT101 potentiostat/galvanostat and NOVA software) system with a 0.1 M tetrabutylammonium hexafluorophosphate (TBAHFP) solution in anhydrous acetonitrile (CH_3CN) as the supporting electrolyte, at a scan rate of 30 mV s^{-1}. The electrolyte was degassed by bubbling N_2 for 20 minutes, and N_2 was injected over the solution before measurements. An ITO substrate coated with samples, an Ag/AgCl electrode, and

platinum graze wrapped around a platinum wire were used as the working, reference, and counter electrodes, respectively. Prior to measure the HOMO and LUMO energy levels of the organic semiconductor films, potentials were referenced to ferrocenium/ferrocene ($FeCp2^{+/0}$) couple by using ferrocene as an internal standard.

External quantum efficiency (EQE) and absorbance:
The EQE spectra were measured using a QE measurement system (Bentham IL1 with Bentham 605 stabilized current power supply) coupled to monochromatic light from a tungsten-halogen light source with a chopping frequency of 300 Hz. The incident photon on the samples was calibrated using a UV-enhanced silicon photodiode. Long-pass filter at 590 nm was used to filter out scattered light from second-order diffraction. The UV–visible absorption spectra were obtained by UV-visible spectrometer (PerkinElmer Lambda 25).

Photoluminescence (PL): The PL spectra were measured with a Fluorolog-3 spectrofluorometer (Horiba Jobin Yvon). All film samples were spin-coated on glass substrates

Transient absorption spectroscopy (TAS):
Samples for TAS were spin-coated onto glass using the same conditions as for solar cells. The spin-coated films were excited at 600 nm. Sub-picosecond TAS was carried out at 800 nm laser pulse (1kHz, 90 fs) by using a Solstice (Newport Corporation) Ti:sapphire regenerative amplifier. A part of the laser pulse was used to generate the pump laser at 600 nm, with a TOPAS-Prime (light conversion) optical parametric amplifier. The other laser output was used to generate the probe light in near visible continuum (450–800 nm) by a sapphire crystal. The spectra and decays were obtained by a HELIOS transient absorption spectrometer (450–1,450 nm) and decays to 6 ns. The samples were measured in N_2 atmosphere.

Charge extraction and transient photovoltage (CE/TPV):
In CE, the desired light intensity range from ~ 0.1 to 10 Sun equivalent is provided by with 12 LEDs connected to a remote-controlled power supply. The LEDs are turned on for several 100 ms to allow the device to reach to steady states. Due to the rise/fall time of LEDs is around 100 ns, the time resolution is limited for testing those fast response diode such as inorganic photodetectors (response time of these fast detector is usually on ns scale). The voltage source used here was a Keithley 2400 source meter and is used to set. The transients are acquired with a DAQ card connected to a TDS 3032 Tektronik digital storage oscilloscope triggered in parallel with the cell switch gate signal from the DAQ. In the TPV setup, the device is connected to the oscilloscope with a high impedance of 1 MΩ to ensure the V_{oc} condition, the device was held at open-circuit condition under different background light intensity controlled by a ring of LEDs as described before; then a small optical excitation was provided by a pulsed Continuum Minilite Nd:YAG laser at 532 nm with a pulse width of smaller than10nm. This small excitation produced a small voltage transient decay was then measured on the oscilloscope was fitted with a mono-exponential to obtain the small perturbation carrier lifetime and finally to be used to estimate the total charge carrier lifetime within the device.

Ambient photoemission spectroscopy (APS):
APS measurements are utilizing the APS04 system from KP Technology. The samples are prepared as thin films, neatY6, BTP-4Cl, PM6 and blends of PM6 to either Y6 or BTP-4Cl, on top of ITO in device thickness. Samples are grounded through ITO throughout the measurement. The samples are irradiated by UV light (4.4eV to 6.2eV) through the monochromator. The photoemitted electrons from the sample generate radicals with air which are further collected by the positively biased tip. The cube root of the photoemission signals were linearly fitted to

extract the HOMO energy values and the tail states are calculated by integrating the signals below the HOMO onset.

Density functional theory (DFT) calculation:
DFT calculations were carried out on the Imperial College High-Performance Computing Service using Gaussian09 software[1] at the B3LYP level of theory and with a basis set of 6-31G(d,p).[2-5] Energy scans were constructed by freezing the dihedral in question at different angles and allowing structural relaxation to the lowest energy at each angle. Alkyl side chains are simplified to methyl groups to reduce computational time.

[1] M. J. Frisch, G. W. Trucks, H. B. Schlegel, G. E. Scuseria, M. A. Robb, J. Cheeseman, G. Scalmani, V. Barone, B. Mennucci, G. A. Petersson, H. Nakatsuji, M. Caricato, X. Li, H. P. Hratchian, A. F. Izmaylov, J. Bloino, G. Zheng, J. L. Sonnenberg, M. Hada, M. Ehara, K. Toyota, R. Fukuda, J. Hasegawa, M. Ishida, T. Nakajima, Y. Honda, O. Kitao, H. Nakai, T. Vreven, J. A. Montgomery Jr., J. E. Peralta, F. Ogliaro, M. Bearpark, J. J. Heyd, E. Brothers, K. N. Kudin, V. N. Staroverov, R. Kobayashi, J. Normand, K. Raghavachari, A. Rendell, J. C. Burant, S. S. Iyengar, J. Tomasi, M. Cossi, N. Rega, J. M. Millam, M. Klene, J. E. Knox, J. B. Cross, V. Bakken, C. Adamo, J. Jaramillo, R. Gomperts, R. E. Stratmann, O. Yazyev, A. J. Austin, R. Cammi, C. Pomelli, J. W. Ochterski, R. L. Martin, K. Morokuma, V. G. Zakrzewski, G. A. Voth, P. Salvador, J. J. Dannenberg, S. Dapprich, A. D. Daniels, O. Farkas, J. B. Foresman, J. V. Ortiz, J. Cioslowski, D. J. Fox, Gaussian 09, Revision A.1, Gaussian, Inc., Wallingford, CT 2009.
[2] A. D. Becke, J. Chem. Phys. 1993, 98, 5648.
[3] G. A. Petersson, M. A. Al-Laham, J. Chem. Phys. 1991, 94, 6081.
[4] G. A. Petersson, A. Bennett, T. G. Tensfeldt, M. A. Al-Laham, W. A. Shirley, J. Mantzaris, J. Chem. Phys. 1988, 89, 2193.
[5] P. J. Stephens, F. J. Devlin, C. F. Chabalowski, M. J. Frisch, J. Phys. Chem. 1994, 98, 11623

Corrected photocurrent (J_{ph}) measurement:
The corrected photocurrent applied is a pulsed measurement. The voltage pulse is provided by a Keithley 2400 source meter and has a width of ~ 2 ms, within which a dark current is measured before a ~ 1 ms light pulse provided from the ring of 12 white LEDs (used throughout the transient measurements) controlled via a fast switching MOSFET allows the corresponding light current to be measured. The current is measured across a known resistance on a Tektronix TDS3032B oscilloscope.

Supplementary Notes:

Note 1:

In practice, organic semiconductors used in optoelectronic devices are not ideal as a result of the disorder in molecular conformation (orientations of the molecular backbone), intermolecular interactions (the torsion of adjacent molecules caused by charge carriers), and the presence of chemical or other defects. This disorder results in intra sub-band energy states lying between the conduction and valence bands, which are also called tail states.

It has also been suggested that the tail states distribution exponentially (shown in Figure 2.1) decays towards into the bandgap (similar to the tail of a Gaussian distribution below the band edges). The density of conduction band tail states N_{CBT} can be written as

$$N_{CBT} = N_{0CBT}\exp\left(\frac{E_{Fn} - E_C}{E_{chC}}\right) \quad (1)$$

Where the $N_{0\mathrm{CBT}}$ is the effective density at the conduction band edge, E_{Fn} is the quasi-Fermi level of electron, E_{C} is the energy of conduction band edge and E_{chC} is the characteristic slope of the conduction band tail. The density of valence band tail states can be written analogously as

$$N_{VBT} = N_{0VBT}\exp\left(\frac{E_V - E_{Fp}}{E_{chV}}\right) \quad (2)$$

Where the $N_{0\mathrm{CBV}}$ is the effective density at the valence band edge, E_{V} is the energy of valence band edge, E_{Fp} is the quasi-Fermi level of hole, and E_{chV} is the characteristic slope of the valence band tail.

In a charge extraction experiment conducted at open-circuit conditions, a solar cell is held at a certain light bias before the light is switched off at the same time as the voltage is switched to short circuit. The charge carriers that were electrically and optically injected into the solar cell are then extracted. The charge carrier density can be extracted increases exponentially depends on the quasi-Fermi level splitting and the shape of tail states that accumulate charge carriers. which can determine a relationship as follow

$$\mathrm{n} = n_0\exp\left(\gamma V_{oc}\right) \quad (3)$$

Where n_0 and γ are the fitting parameters of charge carrier density n as a function of V_{OC}. For organic solar cells in the absence of contact losses, V_{OC} will track the quasi-Fermi level in the bulk ($qV_{\mathrm{OC}} \cong \Delta E_{\mathrm{F}} = E_{\mathrm{Fn}} - E_{\mathrm{Fp}}$). Thus the exponential slope of γ directly relates to the distribution of tail states described in Equation 1 & 2, where the averaged tail state characterisation energy E_{ch} (assuming $E_{\mathrm{chC}} = E_{\mathrm{chV}}$) can be determined from γ via

$$E_{ch} = \frac{1}{2\gamma} \quad (4)$$

Thus, the relationship between charge carrier density extracted at V_{OC} (quasi-Fermi level splitting ΔE_{F}) and tail state characterisation energy E_{ch} can be described as follow:

$$\mathrm{n} \propto \exp\left(\frac{\Delta E_F}{2E_{ch}}\right) \quad (5)$$

Note 2:

The relationship between charge carrier recombination rate R and charge carrier density n at open circuit follows a power law according to

$$R = \frac{dn}{dt} = k_0 n^{\delta} \tag{6}$$

Where k_0 is the recombination rate constant independent to charge carrier density, δ is the reaction order of recombination determined via $\delta = d\log(R)/d\log(n)$. For an ideal bimolecular recombination process of a free electron recombines with a free hole, the reaction order should equal to 2. However, in practice, we normally observe an empirical reaction of organic solar cells is higher than 2. Thus, the relationship between recombination rate and charge carrier density can be also expressed as a pseudo second order process as follow

$$R = \frac{dn}{dt} = k_{bi}^{*} n^2 \tag{7}$$

Where k_{bi}* is the effective bimolecular recombination coefficient determined via $k_{bi}* = k_{bi} n^{\delta-2}$. For a pure bimolecular process, k_{bi}* should be independent to charge carrier density.

In the presence of sub-bandgap tail states, most photo-generated charge carriers will be trapped into these states (if the device is operated much below the band-edges). Assuming recombination results primarily from the recombination of a free carrier with a trapped carrier (e.g (n_{free} and p_t) as

$$R \propto n_{free} p_t \propto \exp\left(\frac{\Delta E_F}{2kT}\right) \exp\left(\frac{\Delta E_F}{2E_{ch}}\right) \tag{8}$$

Thus, we can use equation 6 and 8 to derive the reaction order via

$$\delta = \frac{E_{ch}}{kT} + 1 \tag{9}$$

For E_{ch} = 25 meV, δ = 2, corresponding to ideal behaviour.

A theoretical prediction of bimolecular recombination of free charge carriers is by Langevin bimolecular recombination. Assuming that the free carriers are generated independently, their recombination is random and ideally of second order from a kinetic point of view. It can be considered a mobile hole and a fixed electron, the hole drifts towards the electron driven the Coulomb attraction only, creating an electric field that interacts with the hole as following:

$$F = \frac{q}{4\pi\varepsilon_r\varepsilon_0 r^2} \tag{10}$$

Where q is an elementary charge, ε_r is the relative permittivity, ε_0 is the vacuum permittivity, and r is the electron-hole distance. The corresponding drift current for hole is:

$$J = qp\mu F = \frac{p\mu q^2}{4\pi\varepsilon_r\varepsilon_0 r^2} \tag{11}$$

Where p is the hole density, and μ is the mobility. As a result, the recombination current I_{rec} of the holes flowing into a single sphere around the fixed electron becomes:

$$I_{rec} = J4\pi r^2 = \frac{p\mu q^2}{\varepsilon_r\varepsilon_0} = k_{Langevin} qp \tag{12}$$

Where the $k_{Langevin}$ is Langevin bimolecular recombination rate constant.

With the general definition of the Langevin recombination rate shown in Equation 10-12, if the two carriers have substantially different local mobilities, the recombination rate is determined by the faster carrier. It is widely applied in literature by the equation $k_{\text{Langevin}} = (\mu_h + \mu_e)q/\varepsilon_r\varepsilon_0$, assuming the recombination contributed by the movement of both charge carriers (for example reference 15 by Neher et al.). However, in the bulk heterojunction, the bulk recombination event happens at the donor/acceptor interface. In this context, the limiting step for the two charges of opposite polarity to meet may be determined by the slow carrier joining the heterojunction, thus leading to $k_{\text{Langevin}} = q\mu_{\text{slow}}/\varepsilon_r\varepsilon_0 \cong q\mu^*/\varepsilon_0\varepsilon_r$. This equation is employed in the analysis herein, where our measured effective mobility determines the averaged charge carrier mobility, explaining the difference in Langevin reduction factor determined in our study and that of Neher et al.

Note 3:

The changes occuring in the Raman spectra upon prolonged laser excitation for IDTBR are associated with increasing torsion angle between the electron donating and accepting groups, and the reader is directed to our study in reference 65 for more details on this. Similarly to IDTBR, we have reason to believe, by a combination of *in situ* degradation studies and DFT simulations, that ITIC also undergoes conformational change upon prolonged photoexcitation. This is the subject of ongoing work which looks more specifically at the degradation of ITIC, and will be published soon.

Supplementary Figures:

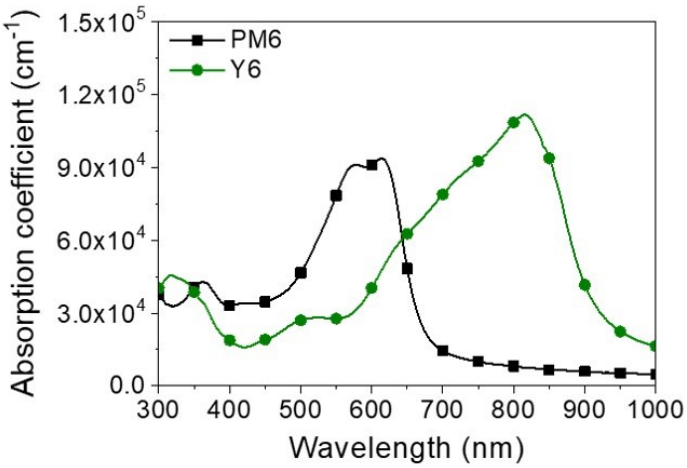

Fig. S1. Absorption coefficients of the PM6 and Y6 in thin films determined from UV-Vis measurements.

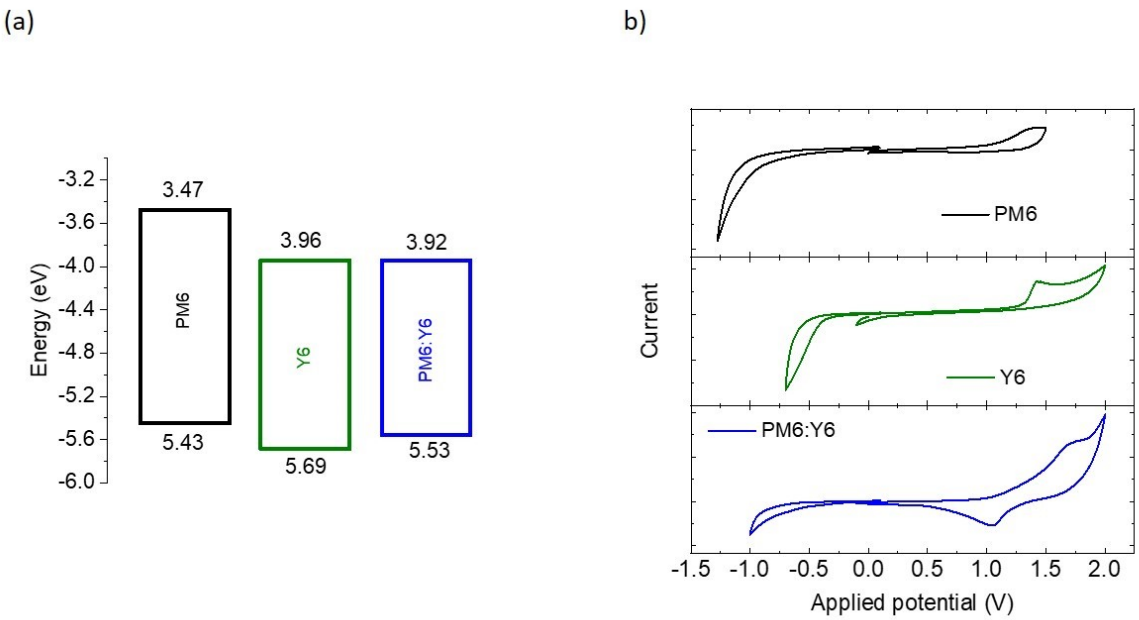

Fig. S2. Materials energetics. (a) Schematic energy level diagram of PM6, Y6 and PM6:Y6 measured by cyclic voltammetry (CV) measurements. (b) CV plots of PM6, Y6, and PM6:Y6 in thin films. We note that energetic values in this work are slightly different from the previous results which might be originated from the 'batch-to-batch' variation and experimental conditions.[1-3]

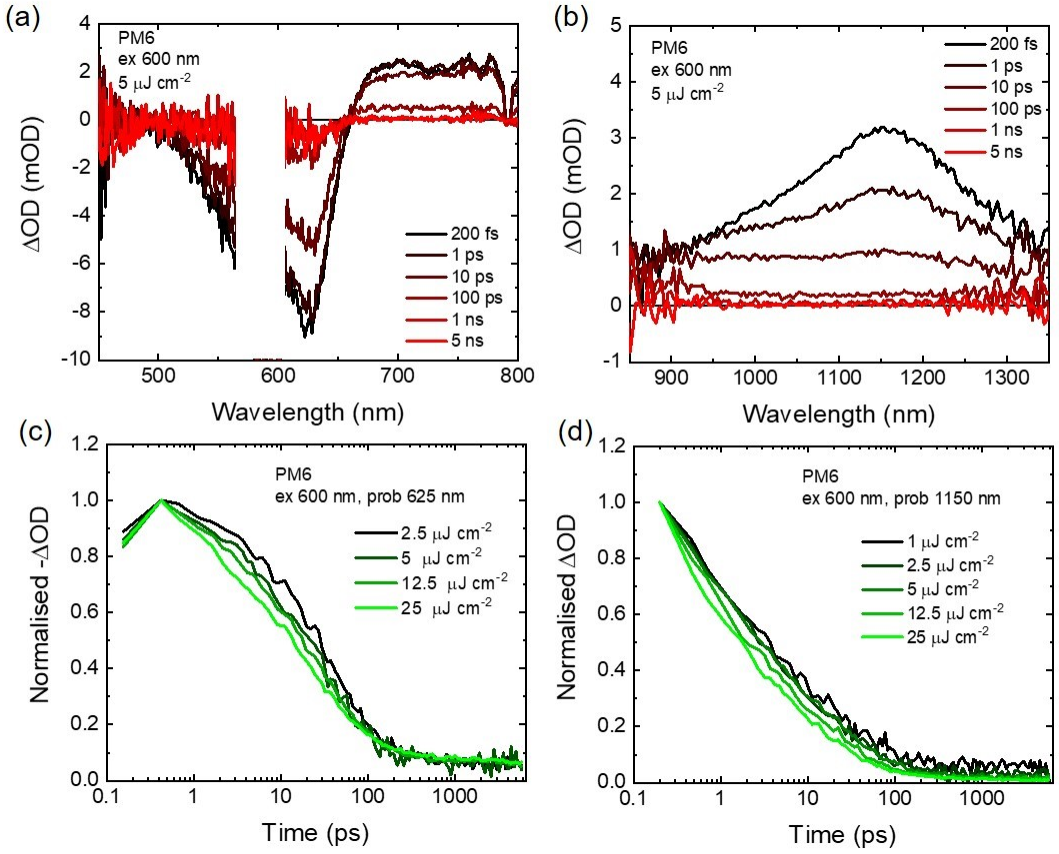

Fig. S3. Transient absorption spectra of neat PM6 film excited at 600 nm and probed at (a) visible region and (b) near IR region. Transient absorption decay dynamics for neat PM6 film excited at 600 nm and probed at (c) 625 nm and (d) 1150 nm, respectively.

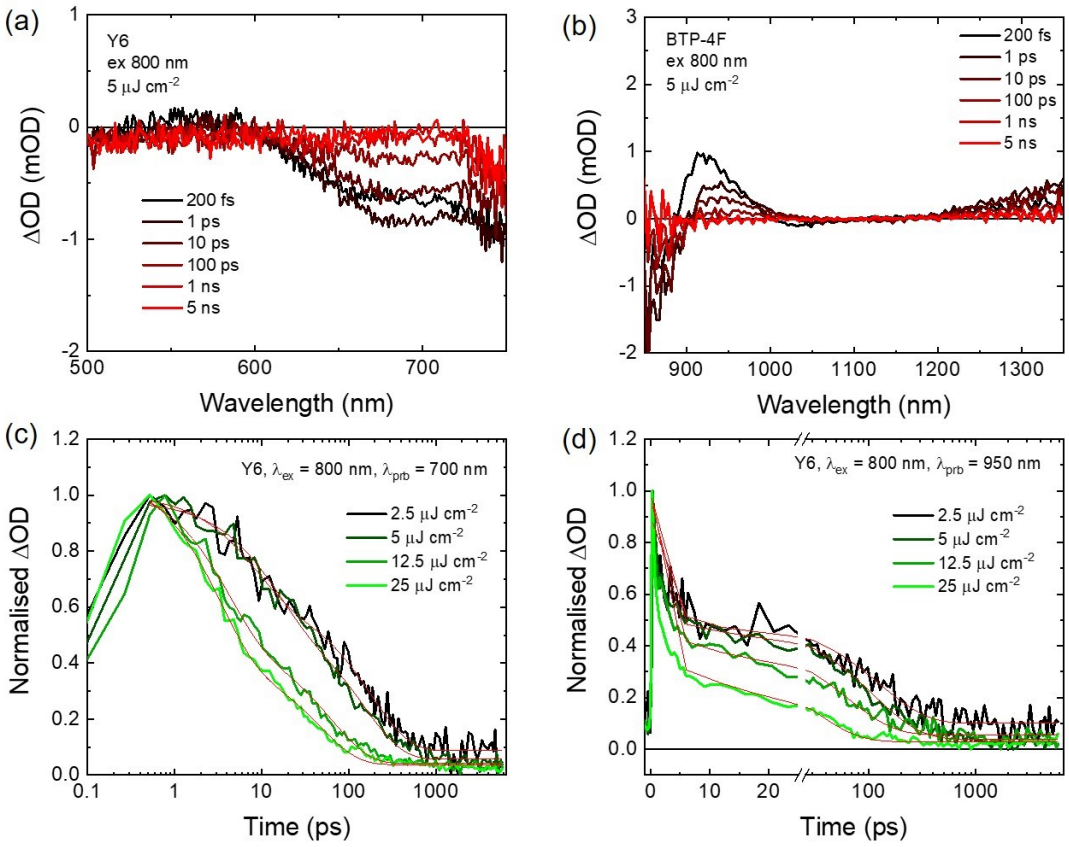

Fig. S4. Transient absorption spectra of neat Y6 film excited at 800 nm and probed at (a) visible region and (b) near IR region. Transient absorption decay dynamics for neat Y6 film excited at 800 nm and probed at (c) 700 nm and (d) 950 nm, respectively as a function of excitation density. The red solid lines are biexponential fitting. These transient absorption spectra are primarily assigned to singlet excitons. The acceleration of decay kinetics at high excitation densities is assigned to exciton / exciton annhilation. The negative feature around 600 - 750 nm can be largely attributed to ground-state bleaching, with an approximately monoexponential decay at low excitation density (2.5 μJ cm^{-2}) of 48 ps. The transient absorption spectra also features an excitonic photoinduced absorption peak around 950 nm. The decay of this 950 nm absorption is clearly biphasic. The origin of this biphasic behaviour is unclear, but may be associated with exciton relaxation dynamics and / or the formation of charge transfer excitons / separated charges. We note that nanosecond emission decay kinetics have very recently been reported for Y6 from TCSPC measurements.[4] This may be also be related to the biphasic behaviour observed herein. We note the fast (48 ps) decay observed herein is too fast to be readily observable in most TCSPC measurements.

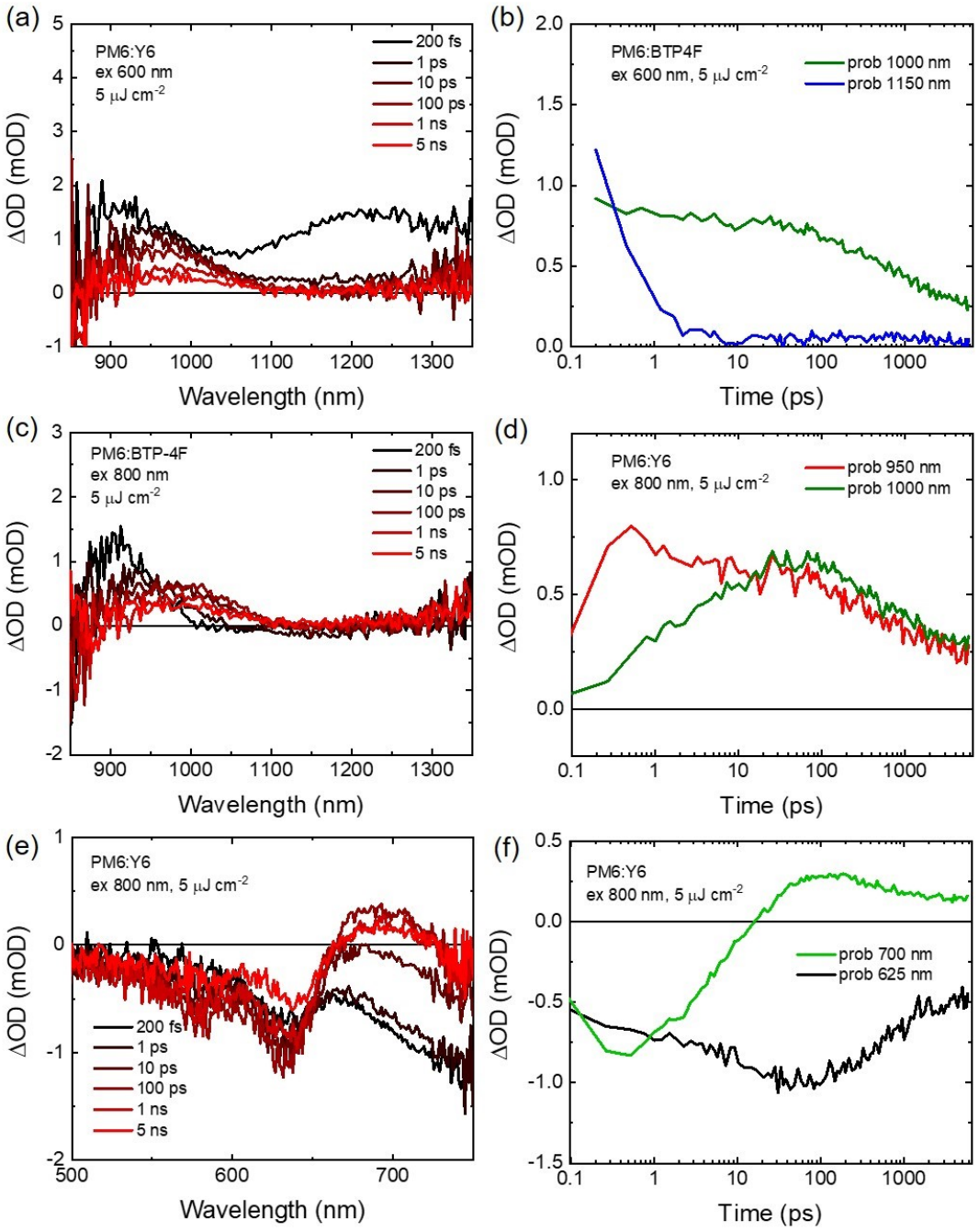

Fig. S5. Transient absorption spectra of PM6:Y6 blend film (a) excited at 600 nm and (b) kinetics probed at 1100 nm and 1150 nm. Transient absorption spectra of PM6:Y6 blend film (c) excited at 800 nm and (d) kinetics probed at 950 nm and 1000 nm. Transient absorption spectra of PM6:Y6 blend film (e) excited at 800 nm and (f) kinetics probed at 625 nm and 700 nm. The photoinduced absorption features at 700 and 1000 nm are assigned to CT / charge separated states, with the rise of these features (8 ps half-times for both wavelengths) following Y6 excitation at 800 nm assigned to hole transfer from Y6 to PM6. The longer timescale decays (half-times of ~ 500 ps) are tentatively assigned to CT state decay due to to geminate recombination[5] and / or dissocation into free charges.

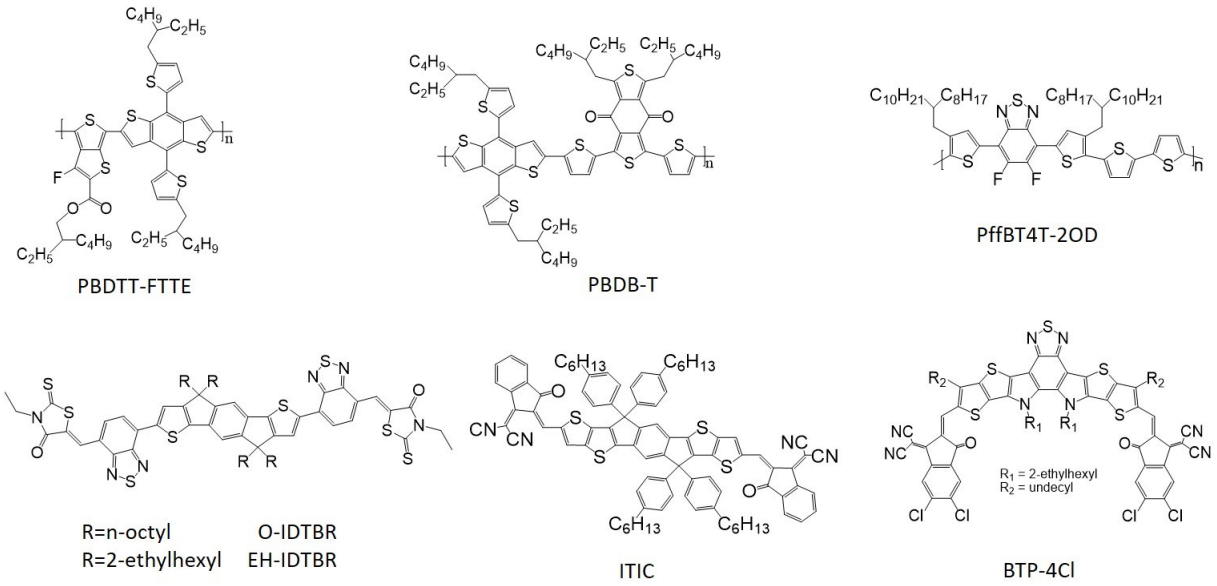

Fig. S6. Molecular structures of the matierials used shown in Figure 3.

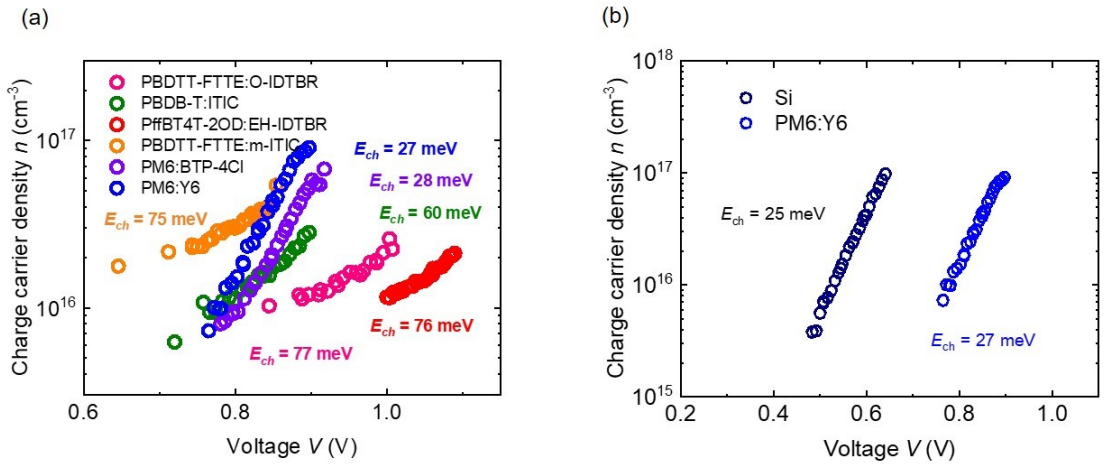

Fig. S7. Charge carrier density of a series of NFA based OSCs and Si device measured by transient charge extraction results at open-circuit condition.

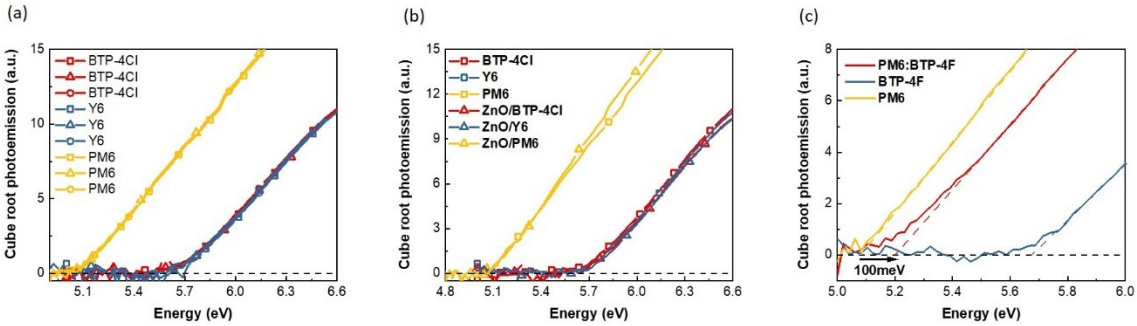

Fig. S8. The photoemission spectra of PM6, Y6, BTP-4Cl (a) on ITO substarte showing APS reproducibility, (b) on ZnO layer confirming no effect of underneath layer on energetics and (c) PM6:Y6 blend film compared to PM 6 and Y6 neat films. ~100 meV band edge shift and increase in the tail states of PM6 polymer upon blending with Y6 acceptors.

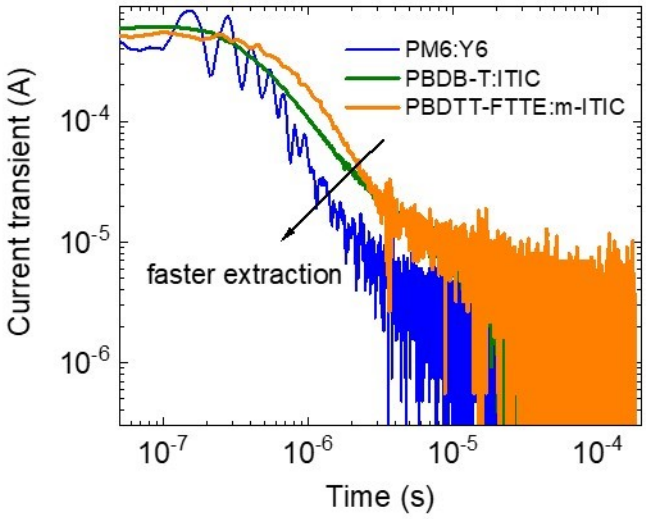

Fig. S9. Current extraction transient of PM6:Y6, PBDB-T:ITIC and PBDTT-FTTE:m-ITIC devices measured at short-circuit condition.

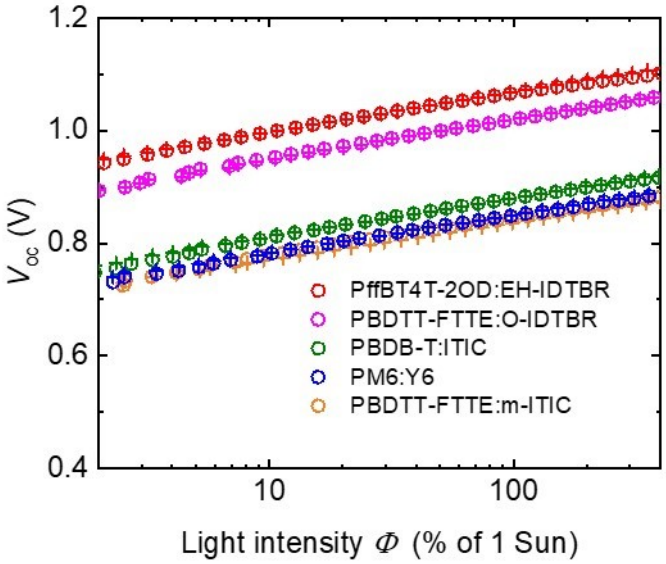

Fig. S10. Measured V_{OC} (open circles) and reconstructed V_{OC} as a function of light illumination intensities of PffBT4T-2OD:EH-IDTBR, PBDTT-FTTE:O-IDTBR, PBDB-T:ITIC, PM6:Y6 and PBDTT-FTTE:m-ITICdevices.

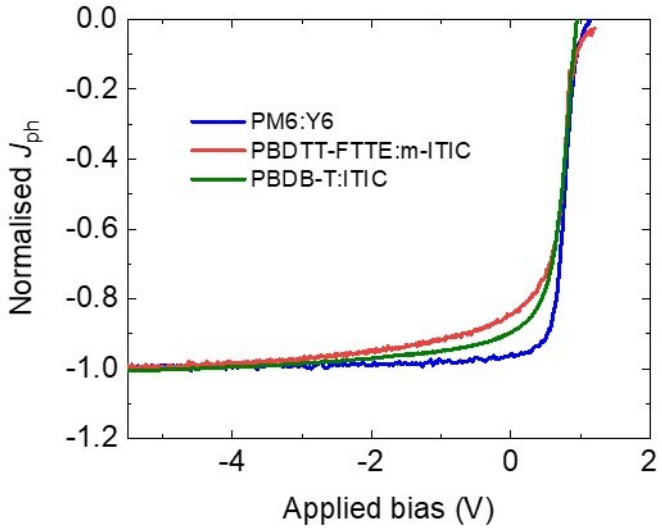

Fig. S11. Corrected photocurrent J_{ph} of PM6:Y6, PBDTT-FTTE:m-ITIC and PBDB-T:ITIC devices, the photocurrent is normalised.

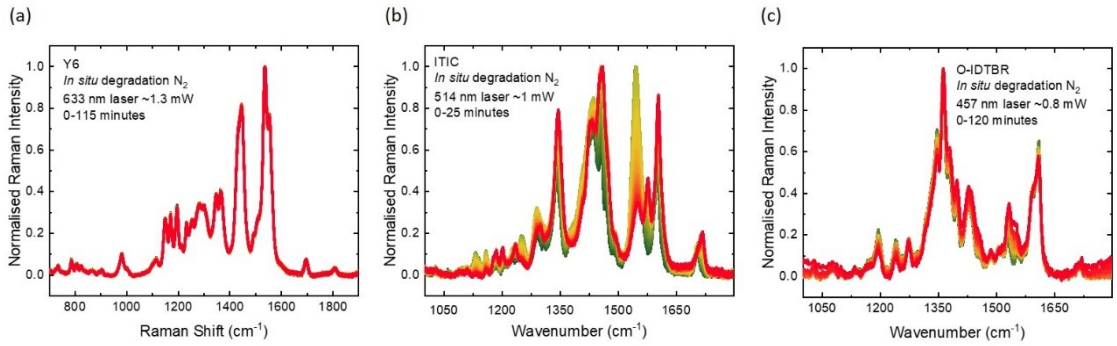

Fig. S12. Baseline backgound corrected and normalised in situ resonant Raman spectra (a) at 633 nm excitation of a neat Y6 film, (b) at 514 nm excitation of a neat ITIC film, (c) at 457 nm excitation of a neat IDTBR film shown as a function of laser irradiation time starting with green spectra and progressing to red. Different laser wavelengths were used to acheive resonant accelarated excitation of each NFAs. The films are kept under a high nitrogen flow to minimise photo-oxidation.

Table S1. Calculated exciton diffusion length of PM6 and Y6 at various energy density. n_0: exciton density, $t_{1/2}$: half-lifetime of exciton probed at 625 nm for PM6 and 950 nm for Y6. k: exciton intrinsic decay rate constant, γ: EEA rate coefficient, α: modify factor, D: diffusion coefficient and L_d: diffusion length.

Donor PM6

Energy μJ cm^{-2}	n_0 ($\times10^{18}$)	$t_{1/2}$ ps	k	α	γ ($\times10^{-9}$) cm^3 s^{-1}	D cm^2 s^{-1}	L_d nm
2.5	0.89	28	2.48×10^{10}				
5	1.8	21		0.75	6.5	0.0018	2.24
12.5	4.4	17		0.60	5.1	0.0014	1.98
25	8.9	13		0.46	4.6	0.0013	1.87

Acceptor Y6

Energy μJ cm^{-2}	n_0 ($\times10^{18}$)	$t_{1/2}$ ps	k	α	γ ($\times10^{-9}$) cm^3 s^{-1}	D cm^2 s^{-1}	L_d nm
2.5	1.2	48	1.44×10^{10}				
5	2.4	32		0.67	0.42	0.001	2.4
12.5	5.9	8		0.17	1.75	0.005	4.8
25	11.8	5		0.10	1.5	0.004	4.5

References

[1] J. Yuan, Y. Q. Zhang, L. Y. Zhou, G. C. Zhang, H. L. Yip, T. K. Lau, X. H. Lu, C. Zhu, H. J. Peng, P. A. Johnson, M. Leclerc, Y. Cao, J. Ulanski, Y. F. Li, Y. P. Zou, *Joule* **2019**, *3*, 1140.

[2] Y. Cui, H. Yao, J. Zhang, T. Zhang, Y. Wang, L. Hong, K. Xian, B. Xu, S. Zhang, J. Peng, Z. Wei, F. Gao, J. Hou, *Nat. Commun.* **2019**, *10*, 2515.

[3] A. Karki, J. Vollbrecht, A. L. Dixon, N. Schopp, M. Schrock, G. N. M. Reddy, T. Nguyen, *Adv. Mater.* **2019**, *31*, 1903868.

[4] L. Zhan, S. Li, T.-K. Lau, Y. Cui, X. Lu, M. Shi, C.-Z. Li, H. Li, J. Hou and H. Chen, *Energy Environ. Sci*., **2020**, 13, 635–645.

[5] L. Perdigón-Toro, H. Zhang, A. Markina, J. Yuan, S. M. Hosseini, C. M. Wolff, G. Zuo, M. Stolterfoht, Y. Zou, F. Gao, D. Andrienko, S. Shoaee and D. Neher, *Adv. Mater.*, 2020, **32**, 1906763.